Prelaunch Radiometric Calibration and Uncertainty Analysis of Landsat Thermal Infrared Sensor 2

Aaron Pearlman, *Member, IEEE*, Matthew Montanaro, Boryana Efremova, Joel McCorkel, Brian Wenny, *Member, IEEE* , Allen Lunsford, and Dennis Reuter

***Abstract*— The Thermal Infrared Sensor-2 (TIRS-2) that will be onboard Landsat 9 has undergone a prelaunch testing campaign to characterize its radiometric, spectral, and spatial performances and demonstrate compliance to its requirements. This work reviews the key elements of the instrument-level radiometric testing using an SI-traceable source to derive its uncertainties. Those arising from on-orbit calibration using the TIRS-2 onboard blackbody are also discussed. We use a Monte Carlo approach to propagate the uncertainties through a nonlinear calibration equation and address both random and systematic uncertainty terms. Achieving the required performance demonstrates the instrument's potential for enhancing our understanding of the Earth's environment.**

***Index Terms*— Calibration, Landsat 9, prelaunch testing, spectral response, Thermal Infrared Sensor 2 (TIRS-2), uncertainty.**

I. TIRS-2 Instrument and Requirement Overview

THE Thermal Infrared Sensor-2 (TIRS-2), expected to launch on Landsat 9 in 2021, will continue the Landsat Program's legacy of providing a moderate-resolution thermal imagery over almost four decades. Scientists use the thermal imagery provided by the Landsat satellites for a wide variety of environmental applications such as cloud detection and masking [1], [2], evapotranspiration studies [3], [4], water use assessments [5], urban heat flux mapping [6], [7], burned area mapping [8], and vectorborne illness potential identification [9], [10]. Many of these applications are enabled through the land-surface-temperature retrievals from the thermal imagery. TIRS-2, which is a functional copy of TIRS, its predecessor on Landsat 8 [11], has two bands at 10.8 and 12.0 μm, enabling more accurate retrievals than the previous Landsat thermal sensors, where only a single channel was available [12].

Manuscript received February 21, 2020; revised April 7, 2020, May 13, 2020, and June 8, 2020; accepted July 8, 2020. Date of publication July 24, 2020; date of current version March 25, 2021. This work was supported by the Landsat Program. *(Corresponding author: Aaron Pearlman.)*

Aaron Pearlman and Boryana Efremova are with GeoThinkTank LLC, Washington, DC 20009 USA (e-mail: aaron@geothinktank.com).

Matthew Montanaro is with the Rochester Institute of Technology, Rochester, NY 14623 USA.

Joel McCorkel and Dennis Reuter are with Goddard Space Flight Center, Greenbelt, MD 20740 USA.

Brian Wenny is with Science Systems and Applications, Inc., Lanham, MD 20706 USA.

Allen Lunsford is with American University, Washington, DC 20016 USA.

Color versions of one or more of the figures in this article are available online at https://ieeexplore.ieee.org.

Digital Object Identifier 10.1109/TGRS.2020.3008655

TABLE I
TIRS/TIRS-2 Parameters

Parameter	TIRS/TIRS-2 requirement	TIRS performance
NEdT @ 300 K (K)	<0.4	0.05 [17]
NEdL ($W/m^2/sr/\mu m$)	<0.059, 0.049	0.008 [17]
Absolute radiometric accuracy (%)	$< 2, 4$	1 [18] *

NEdL values denote the 10.8 μm and 12.0 μm channels, respectively and radiometric accuracy values refer to the nominal brightness temperature range of (260-330 K) and extended range (240-260, 330-360 K), respectively.
*With stray light correction implemented

A comprehensive survey of the applications enabled by land-surface-temperature retrievals can be found in [13].

TIRS-2 will produce a radiometrically SI-traceable, geolocated thermal imagery of the Earth with the same parameters as Landsat 8 TIRS: 16-day repeat, 100-m spatial sampling (resampled to 30 m in the final product), 185-km swath width, and 70 frames/s operation. The instrument is a pushbroom sensor with a 15° cross-track field of view with the same basic architecture as TIRS but with some improvements such as increased electrical redundancy and improved stray-light suppression [14]. It has a f/1.6 four-lens telescope that focuses onto three quantum-well infrared photodetector (QWIP) arrays usually termed sensor chip assemblies (SCAs) [15], an onboard blackbody for calibration, and a scene-select mirror for switching among the Earth view, blackbody, and space views (Fig. 1). The onboard calibrator (OBC), the same design as TIRS, is modeled after the blackbodies used as part of other heritage systems: the Visible Infrared Radiometer Suite (VIIRS) and the Moderate Resolution Imaging Spectroradiometer (MODIS) [16].

The three QWIP arrays are 512 rows × 640 columns each. A filter for each channel covers ∼70 rows of each SCA with an opaque section in between for dark count monitoring (Fig. 1). In its operational mode, only two rows are read out from each channel and dark region. A combination of these detectors from the two rows that meet the performance requirements forms an effective field of view that spans the 185-km swath width and is transmitted to the ground. Those two rows are chosen based on the component- and instrument-level radiometric and spectral characterization tests (discussed in the next section). The primary and redundant rows are combined in the ground processing system to produce the standard Landsat scene image product. Any underperforming

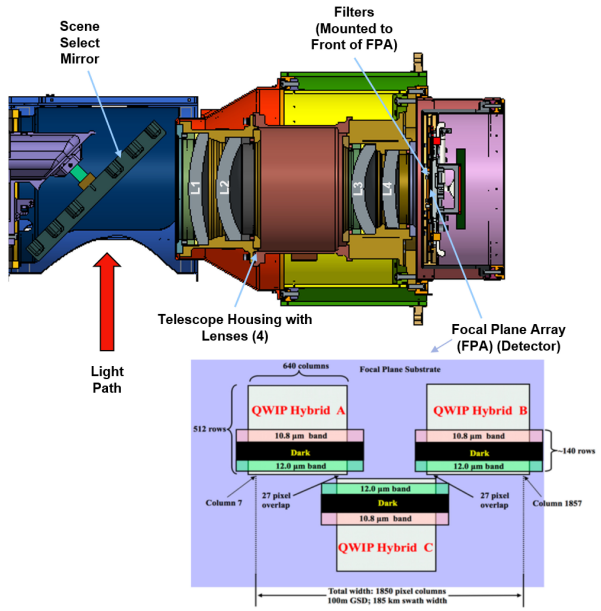

Fig. 1. TIRS-2 schematic with SSM, telescope lenses, and SCA. (Bottom) SCA layout with three QWIP arrays and approximate filter positions for the 10.8- and 12.0-μm channels and dark regions. (Note that the OBC is not included in the figure.)

individual detector from the primary row can be replaced with the corresponding detector in the redundant row to produce a "perfect" row of data for the image product. The two rows may be changed in flight should it become necessary, although the rows have been stable throughout the Landsat 8 mission and a similar performance is expected from Landsat 9.

This work addresses the absolute radiometric uncertainty requirement, interpreted as uncertainty. Table II shows the accuracy and noise requirements for TIRS-2 (and TIRS) and the TIRS on-orbit performance, which is discussed further in [19]. The pairs of numbers either represent the brightness-temperature scene ranges, defined as 260–330 K (nominal range), or 240–260 and 330–360 K (extended range), or correspond to the 10.8-μm channel and 12.0-μm channels, respectively. Note that a 2% radiometric uncertainty in the nominal range corresponds to about 1.2 and 1.9 K in brightness-temperature uncertainty in the two channels, respectively. A 4% radiometric uncertainty in the extended range corresponds to about 3.2 and 3.6 K brightness-temperature uncertainty. The TIRS-2 performance is expected to be comparable with the TIRS performance but with an improved stray-light suppression. Previous studies on TIRS have shown that stray light can impact the radiometric uncertainties beyond the requirement level, but the software-correction methodologies have been implemented in the ground processing system to reduce these uncertainties significantly to meet the requirement [14], [18], [20], [21]. Considering stray-light artifacts as part of the TIRS-2 uncertainty budget would show the uncertainties meeting the requirement. We take a different approach to the requirement in this article, however, and primarily consider the radiometric impacts from the uniform scenes where stray light has no impact. We will leave a detailed discussion on all scatter impacts, both far-field stray-light and near-field stray-light (ghosting) artifacts, for a separate work. This approach is consistent with a more literal interpretation of the requirement, which states its application for the "extended, spatially uniform, unpolarized targets." Before discussing the uncertainty budget, we first present an overview of the relevant prelaunch testing methodologies and results, followed by the uncertainty methodology.

II. Prelaunch Calibration and Characterization

A. Prelaunch Testing Overview

The prelaunch testing—with characterization at various integration phases—follows the best practices established by the remote sensing community [22]. The integration phases include component-level, subassembly-level, instrument-level, and spacecraft-level testings to address the radiometric requirements (including the ones introduced earlier), as well as the spatial, spectral, and geometric requirements [19], [23]. Fig. 2 shows some of the key measurements in all testing phases. Many tests are repeated at different phases to ensure the validity of their results. For instance, the relative spectral response (RSR) is derived independently through the component-level filter transmittance and detector relative response measurements, as well as through the instrument-level measurements to ensure their consistency [24]. Spectral characterization was also performed at the subassembly level in order to refine the test setup and the sampling strategy in advance to the instrument-level characterization (Fig. 2) [25]. The instrument-level spectral measurements provided lower uncertainties in establishing the channel average spectral responses, so they are expected to be used in operations rather than those derived by component-level measurements. Thus, the uncertainties of the instrument-level RSR will be discussed thoroughly here (and those derived by the component-level measurements, considered as a validation, are discussed in [24]).

The radiometry (calibration) measurements were done only at instrument level, since this is the only configuration where the reference blackbody source could be installed and the final instrument electronics were integrated. This full-aperture reference blackbody source called the flood source used for instrument-level testing is the basis for the TIRS-2 radiometric calibration. Its SI traceability was first established for TIRS testing in 2012 and recharacterized for use for the TIRS-2 program in 2018 at the Space Dynamics Laboratory (SDL) [26]. This was done through comparison with a standard blackbody source called the long-wave infrared calibration source (LWIRCS) by an SDL transfer radiometer [27]. The LWIRCS spectral radiance scale is tied to both the NIST-calibrated temperature sensors and the cavity model as well as through the NIST transfer radiometer (TXR) [28]. The effective emissivity of 0.9920 was determined with an uncertainty of 0.0023, which corresponds to the uncertainty in the spectral radiance scale including the TXR transfer uncertainty. The emissivity results showed no significant changes between the 2012 and 2018 measurements. This TIRS-2 response to the flood-source illumination is compared

TABLE II
UNCERTAINTY BUDGET (%)

	Parameter	10.8 μm		12.0 μm	
		Nominal	Extended	Nominal	Extended
Flood Source-Based Terms	Spectral Response	0.050	0.060	0.10	0.15
	Flood Source Temperature	0.067	0.082	0.059	0.072
	Flood Source Calibration	0.20	0.20	0.20	0.20
	Linearization	0.30	0.70	0.040	0.10
	Fitting	0.37	0.41	0.22	0.27
	TIRS-2 Radiometric Reproducibility Bias	0.22	0.22	0.24	0.24
	TIRS-2 Radiometric Reproducibility	0.24	0.24	0.10	0.10
	TIRS-2 Noise	0.0046	0.0054	0.0071	0.0084
OBC-Based Terms	OBC Temperature	0.21	0.36	0.19	0.35
	Fitting	0.27	0.31	0.036	0.065
	OBC Angular Variability	0.020	0.020	0.020	0.020
	TIRS-2 Radiometric Reproducibility Bias	0.071	0.071	0.075	0.075
	TIRS-2 Radiometric Reproducibility	0.34	0.34	0.54	0.54
	Flood Source-OBC Bias	0.42	0.49	0.32	0.40
	Flood Source-OBC	0.20	0.22	0.31	0.32
$k = 1$ **Confidence Intervals**		**U-,U+**	**U-,U+**	**U-,U+**	**U-,U+**
Pre-launch Total		**-0.80, 0.36**	**-1.1, 0.66**	**-0.58, 0.097**	**-0.64, 0.16**
On-board Total		**-1.3, 0.0**	**-1.7, 0.16**	**-1.3, 0.026**	**-1.5, 0.029**

Nominal refers to a brightness temperature range of 260-330 K and extended range refers 240-260 K and 330-360 K. Each bias term is followed by a bias uncertainty term. The figure on the right illustrates the terms contributing to pre-launch and on-orbit uncertainties.

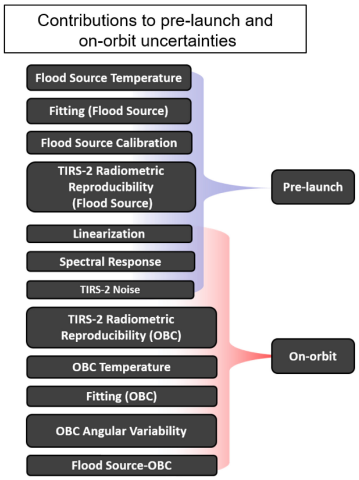

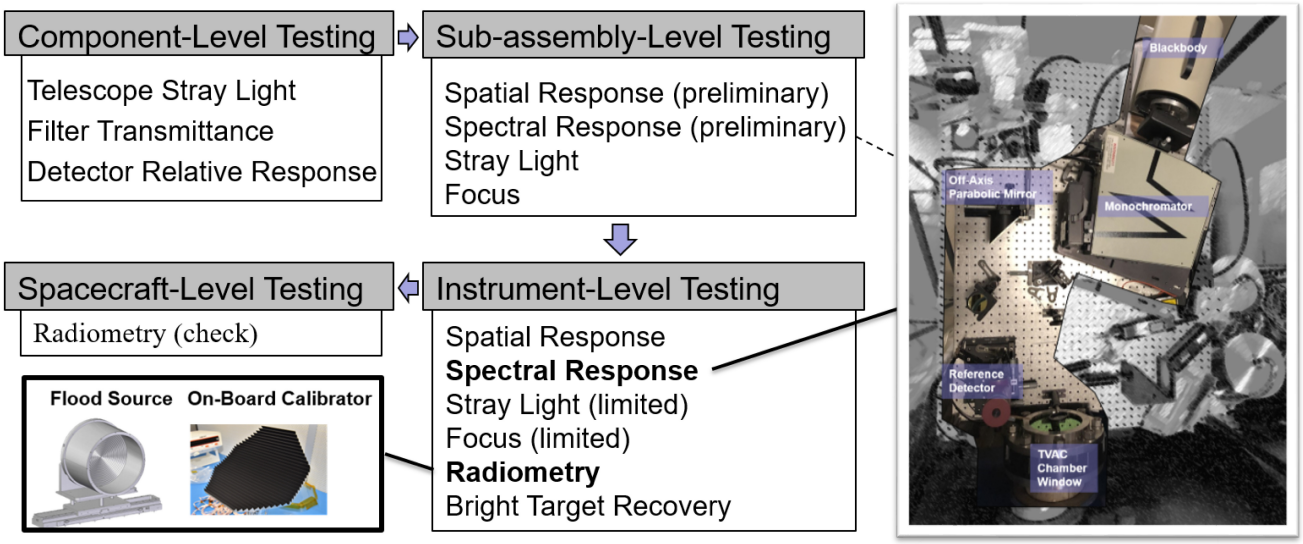

Fig. 2. Overview of prelaunch testing including key measurements at the component-, subassembly-, instrument-, and spacecraft-level testings. The calibration uncertainty is derived from the instrument-level measurements of the RSR and radiometry tests. (Bottom left) SI-traceable flood source and onboard calibrator establish the prelaunch calibration and on-orbit calibration capability. (Right) Blackbody-monochromator setup is used to measure the RSR at both subassembly- and instrument-level test phases.

with the TIRS-2 onboard blackbody illumination to establish an on-orbit calibration capability (Fig. 2).

The instrument-level testing occurred at the Goddard Space Flight Center in two phases with the vibration/acoustic testing performed in-between. Together, these phases verified the stability of the hardware and repeatability of its calibration and RSR results in a simulated on-orbit environment inside a thermal vacuum chamber. The spatial response, stray light, focus, and bright-target recovery tests were also included in this phase. The focus test is done to verify that the image is focused on the detector arrays; the bright target recovery test is done to verify that the detector arrays do not suffer from the image memory artifacts. The scatter and spatial responses characterize the potential image artifacts due to spatial scene nonuniformities. As mentioned, the analysis here will address the radiometric uncertainties arising from the uniform scenes only, where the results from the radiometry and RSR tests are most relevant. The stray-light tests including far-field stray-light and near-field ghosting artifacts are outside the scope of this article [29].

B. Instrument-Level Calibration

During thermal vacuum radiometry (calibration) testing, the flood source illuminates the TIRS-2 aperture at varying blackbody temperature values in the range of 200–360 K to capture the full dynamic range and characterize any nonlinear response. During a calibration sequence, the scene select mirror (SSM) switches among the space view, OBC, and flood source (nadir) view. During each 1-min view of this sequence, two operational detector rows from each band

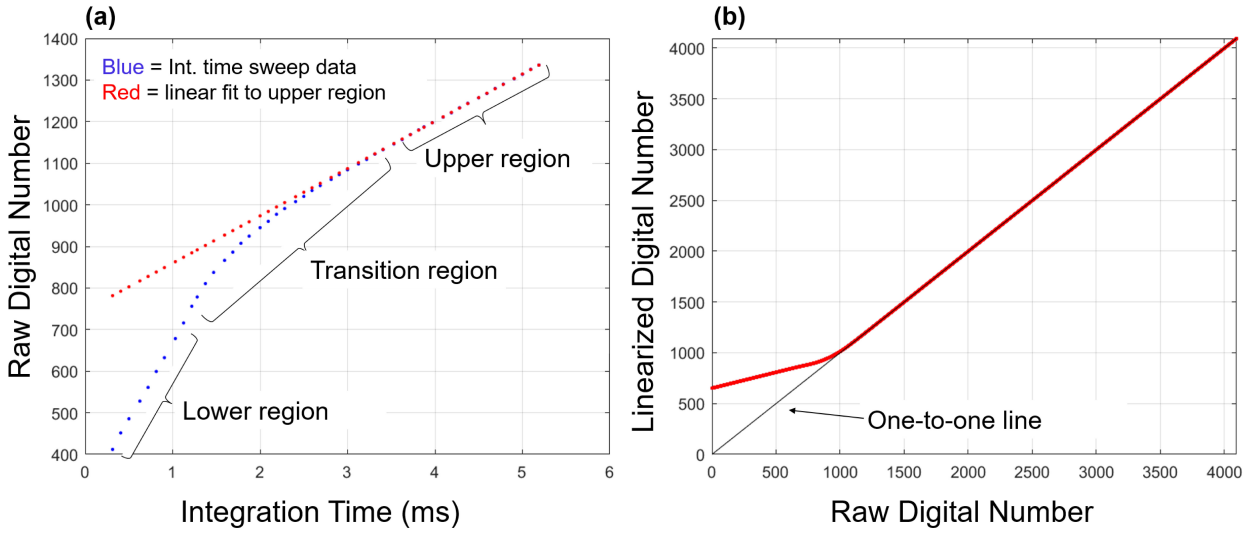

Fig. 3. (a) Integration time sweep showing the bottom, transition, and top regions. The raw counts are converted to match the slope of the top region. (b) Curve shows conversion over the entire range of digital counts.

(10.8 and 12.0 μm, and dark) are read out at 70 Hz to generate 4200 samples per detector. Additional diagnostic modes are available, where almost every detector of each array is read out. In this way, calibration data are obtained for the flood source and OBC for all potential operational detectors. We will discuss one potential approach to on-orbit calibration using the OBC, but the final approach will be determined on-orbit. The space view during testing consists of a cold ($\sim$100 K) target inside the thermal vacuum chamber.

The calibration process described here is similar to that of TIRS discussed in [30]. There are three basic steps in the calibration: linearization, TIRS-2 flood-source-signal retrieval, and the calculation of the flood-source effective spectral radiance. The linearization process is required, because the electronic gain is not constant through its range of digital counts. It has two distinct gains with a transition region between them that are revealed if the integration time is swept while illuminated by a stable radiance (Fig. 3). The signals are linearized so that all digital count values have the same electronic gain.

Both the flood-source view and space view digital counts are linearized and then subtracted to remove the background radiance signal and isolate the flood-source signal ΔC for all detectors at different flood-source temperatures. The blackbody temperature is converted into effective spectral radiance using the Planck function and the RSR—also measured in thermal vacuum testing [24]. A slightly nonlinear model—due to some uncorrected nonlinearity in the linearization process and potential nonlinearity in the photon absorption process itself—is generally used to fit the effective spectral radiance to ΔC. Note that this generates coefficients (or a lookup table) for each detector, but all detectors in a given band use the same RSR. For the purpose of this article, we will model the TIRS-2 calibration with a quadratic dependence on radiance, where L is the effective spectral radiance of the blackbody, ϵ is its emissivity, L_{bk} is a background term representing the difference in background between the blackbody and the space view

$$\epsilon L + L_{bk} = q\Delta C^2 + m\Delta C + b \tag{1a}$$

$$\epsilon L = q\Delta C^2 + m\Delta C. \tag{1b}$$

The background term present in (1a) can justify an offset term in the calibration equation. We neglect this term, however, since the background is small [derived as 0.0039 ± 0.0128 W/m^2/sr/μm and 0.0593 ± 0.0135 W/m^2/sr/μm across all detector columns for the 10.8- and 12.0-μm channels, respectively, using (1a)], and could deviate on-orbit from the thermal vacuum test conditions, to obtain (1b)—our primary calibration equation used in this work.

C. Instrument-Level Relative Spectral Response

The calibration equation uses the channel average RSR to calculate effective spectral radiance. The measurement setup for RSR consists of the setup depicted in Fig. 2 and the custom calibration ground support equipment (GSE) inside the thermal vacuum chamber. The calibration GSE has capabilities to test the radiometric (by the integrated flood source), geometric, and spectral performances of a sensor under the thermal vacuum conditions. There is a special mode designed for spectral measurements, where a beam from the monochromator-based setup outside the thermal vacuum chamber can propagate through the calibration GSE and onto the designated TIRS-2 detectors. The blackbody-monochromator setup consists of a 1000°C blackbody source filling the entrance slit of a monochromator (with 50-lines/mm grating with a blaze wavelength of 12 μm, and a reciprocal dispersion of 78.3 nm/mm). The monochromator output is collimated and directed into the chamber through a ZnSe window and to the TIRS-2 aperture by the calibration GSE optics. The monochromator wavelength is swept through a range of wavelengths covering the desired channel, and at

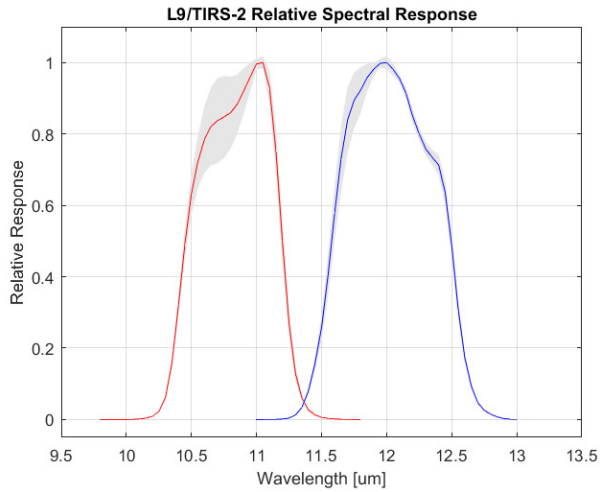

Fig. 4. Average RSR over all SCAs obtained from instrument-level testing for each channel. The shading represents the standard deviation across all locations.

each spectral interval, detector samples are acquired with the monochromator shutter open and close. The latter signal is subtracted from the former to remove the background and obtain the TIRS-2 signal (dn_{TIRS}). A similar wavelength sweep is conducted subsequently with the monochromator output beam directed to a reference detector (liquid nitrogen-cooled HgCdTe detector) with a calibrated relative responsivity (R_{ref}). To separate the blackbody signal from the large ambient background, the blackbody signal is chopped to enable the lock-in amplification of the optical signal. The RSR is derived as

$$\mathrm{SR}_{\mathrm{TIRS}}(\lambda, \mathrm{pix}) = dn_{\mathrm{TIRS}}(\lambda, \mathrm{pix}) \frac{\tau_{\mathrm{ref\,path}}}{\tau_{\mathrm{TIRS\,path}}} \frac{R_{\mathrm{ref}}}{V_{\mathrm{ref}}} \tag{2a}$$

$$\mathrm{RSR}_{\mathrm{TIRS}}(\lambda, \mathrm{pix}) = \frac{\mathrm{SR}_{\mathrm{TIRS}}(\lambda, \mathrm{pix})}{\max_{\lambda}(\mathrm{SR}_{\mathrm{TIRS}}(\lambda, \mathrm{pix}))}. \tag{2b}$$

The dn_{TIRS} with a correction for different optical path transmittances to the reference detector ($\tau_{\mathrm{ref\,path}}$) and to the TIRS-2 aperture ($\tau_{\mathrm{TIRS\,path}}$) is combined with a reference-detector term, R_{ref}, divided by V_{ref}, the reference-detector signal, to generate the spectral response ($\mathrm{SR}_{\mathrm{TIRS}}$). Equation (2b) normalizes the spectral response to arrive at the RSR for each designated region on the detector arrays. The final RSR per channel is derived by averaging over all measured regions to obtain the mean RSR for each channel (Fig. 4).

Further details of the measurements are described in [24] and [25], and an uncertainty budget is included in [25], which we will review in a later section. Once the RSRs were measured, they were used to derive the effective spectral radiance used in the calibration equation.

III. Uncertainty Budget Methodology

This work addresses the TIRS-2 absolute radiometric uncertainty and the SI traceability derived from the measurements described previously. Such uncertainty evaluations have been conducted for the heritage and operational sensors such as VIIRS, MODIS, Geostationary Operational Environmental Satellite (GOES) Imager, and GOES-R series Advanced Baseline Imager (ABI). These sensors generally follow the best practices for establishing SI traceability and uncertainty analysis [31] and have undergone extensive prelaunch testing to characterize their behavior in the operational conditions [32]–[35]. The uncertainty budgets account for the major uncertainty contributors in their calibration equations. Similar parameters were explored (with some added/omitted) based on their unique design attributes and addressed in the calibration. We also follow such best practices by assessing all major uncertainty contributors and include them in the calibration equation. The quality of the fit using the TIRS-2 calibration equation (1b) gives us confidence in this model that forms the basis of the uncertainty budget. The parameters defined in the equation include the fit coefficients, measured signal, and effective spectral radiance of the blackbody given by its temperature sensors, emissivity values, and RSR. These parameters along with additional terms to account for systematic differences from repeated measurements form a comprehensive uncertainty budget.

The parameter uncertainties are propagated through the measurement (calibration) equation (1b) to derive the uncertainty contribution to the radiometric uncertainty expressed with a coverage factor $k = 1$. There are several approaches to propagating uncertainties through a calibration equation: analytically, computationally by perturbation, and computationally by a Monte Carlo approach [36], [37]. The analytical approach refers to using the propagation of the uncertainty formula. The perturbation method refers to perturbing the mean measured value by its uncertainty and propagating through the measurement equation to find the resulting radiometric uncertainty. Both these methods give equivalent results and are used for the VIIRS and MODIS uncertainty analyses, respectively [33], [38].

The drawback of these methods is that they may be less accurate when the measurement equation is nonlinear. Thus, we instead computed the uncertainty contributions by a Monte Carlo computational approach, which does not have such a limitation and is consistent with the established standards for uncertainty analysis [37]. Here, we choose a probability distribution, a Gaussian distribution typically, and generate random numbers with the mean measured value and standard deviation corresponding to its $k = 1$ uncertainty and propagate them through the calibration equation to establish an output distribution of the radiance values. The standard deviation of the resulting radiance values is the radiometric uncertainty. Note that the RSR measurement equations are linear [see (2)], so propagating their uncertainties followed the perturbation approach through the RSR calculation and then converting into effective spectral radiance assuming blackbody illumination. Note that the Monte Carlo approach avoids any inaccuracy due to nonlinearities and gives a convenient way of addressing correlations between the parameters by simply replacing the Gaussian-distributed random numbers with the bivariate-Gaussian-distributed numbers as is done for the highly correlated fitting coefficients [39]. For comparison, the VIIRS analysis in [33] handled correlations by calculating the covariance terms in the uncertainty propagation formula or estimating their upper bounds.

Once the radiometric uncertainties were determined for all parameters, the combined uncertainty u_c is calculated as the root sum squared of the uncertainty components

$$u_c^2(y) = \sum_{n=1}^{N} u_i^2. \tag{3}$$

The uncertainties cannot be combined strictly according to this approach, however, due to some terms involving the uncorrected biases. This leads to some complications in combining the uncertainties. To the best of our knowledge, there have been no other attempts to address the uncorrected bias in the previous prelaunch uncertainty analyses for the satellite sensors. Such biases should be corrected if possible, but this is not realizable for some parameters; thus, such uncorrected biases are often neglected until postlaunch. By including the uncorrected biases, the results can include these terms but remain independent of the correction methodology applied postlaunch. We follow the method described in [40] referred to as the sum uncertainty method (SUMU) to express and combine the uncertainties by adding biases to obtain the combined bias (δ_c), taking the root sum squared of random uncertainties including the bias uncertainties to obtain the combined random uncertainty u_c, and forming a confidence interval corresponding to the total combined $k = 1$ uncertainty

$$U_+ = ku_c - \delta_c$$
$$U_- = ku_c + \delta_c \tag{4}$$
$$y \begin{cases} U_+ \\ -U_- \end{cases}. \tag{5}$$

Most of the uncertainty terms are derived based on the thermal vacuum test data at the nominal (expected on-orbit) conditions. The exceptions are in evaluating calibration reproducibility, where data are taken at instrument temperatures outside the nominal on-orbit conditions to obtain the worst case values. The uncertainties will be expressed for both the nominal and extended brightness-temperature ranges as defined in the requirements.

IV. Uncertainty Results and Discussion

The uncertainty budget is roughly organized into prelaunch and on-orbit uncertainties. The prelaunch uncertainties are associated with the flood-source-based calibration and RSR measurements. Most of the on-orbit uncertainties are tied to the calibration using the OBC (although some flood-source-related terms are included in the combined on-orbit uncertainty as will be discussed). The on-orbit uncertainty total refers to an implementation of the OBC calibration without attempting to make corrections to match the flood-source-based prelaunch calibration.

The flood-source-calibration radiance scale uncertainty was previously discussed in Section II. An additional flood-source-related uncertainty is its temperature uncertainty given by the standard deviation of the mean of its two temperature sensor values in the 200–360 K range. A Monte Carlo method was used to propagate the temperature uncertainty through the calibration equation: The effective spectral radiance values are calculated using Gaussian-distributed temperature values and fitted with the corresponding ΔC to obtain a set of calibration curves (radiance versus ΔC). The uncertainty is calculated by taking the average standard deviation of the radiance at each ΔC and dividing by the radiance. A wide range of radiance values are included to cover the brightness-temperature ranges for comparison with the requirements. The maximum of the nominal and extended ranges is compared with the requirements for operational detectors in all array columns. The average uncertainty (over all detectors) is 0.067% in the nominal range and 0.082% in the extended temperature regions for the 10.8-μm channel and 0.059% and 0.072% in the respective ranges for the 12.0-μm channel.

The calibration using the flood source is also affected by the TIRS-2 count noise, which is approximately the noise (NEDL) divided by the square root of the number of samples. This turns out to be negligible, since the instrument noise is low [10.8-μm channel: 0.005–0.010 W/m^2/sr/μm, 12.0 $-$ μm channel: 0.006–0.010 W/m^2/sr/μm—similar to TIRS performance (Table II)] and a large number of samples are taken (4200 in each flood source and space view). This yields 0.0046% in the nominal range and 0.0054% in the extended temperature regions for the 10.8-μm channel and 0.0071% and 0.0084% in the respective regions for the 12.0-μm channel.

The fitting uncertainty was originally calculated with the perturbation method. The results showed, however, that this method overestimated the uncertainty due to the nonlinear calibration equation. To generate a more accurate fitting uncertainty, we switched to a Monte Carlo methodology while also accounting for the fitting coefficient correlations (calculated using the detectors across all columns). The quadratic fit with confidence intervals for each coefficient corresponding to a $k = 1$ coverage factor is calculated. The random fitting coefficients are generated with a bivariate Gaussian distribution based on these confidence intervals and correlation coefficients. These coefficients are used to generate the calibration curves (radiance as a function of ΔC). This process is illustrated in Fig. 5. The standard deviation of these radiance curves gives the uncertainty. This process is repeated for all operational row detectors and shown in Fig. 6(a). The maximum uncertainty in the nominal and extended brightness-temperature regions is then averaged over the detectors to obtain the final uncertainty values. For the 10.8 μm, the uncertainty is 0.37% (nominal) and 0.41% (extended), and for the 12.0-μm channel, 0.22% (nominal) and 0.27% (extended).

The uncertainty of the linearization process is captured by evaluating its reproducibility. We derive a linearization based on two different sets of calibration data taken at the nominal and nonnominal conditions. The difference between their impacts on radiance gives this additional uncertainty. We found the difference between them to be 0.30% at the nominal and 0.70% at the extended temperature ranges for the 10.8-μm channel, and 0.04% at the nominal and 0.10% at the extended temperature ranges for the 12.0-μm channel. The latter channel is affected less, because the higher count levels in this channel lie on the top section of the linearization curve, where the impact is negligible.

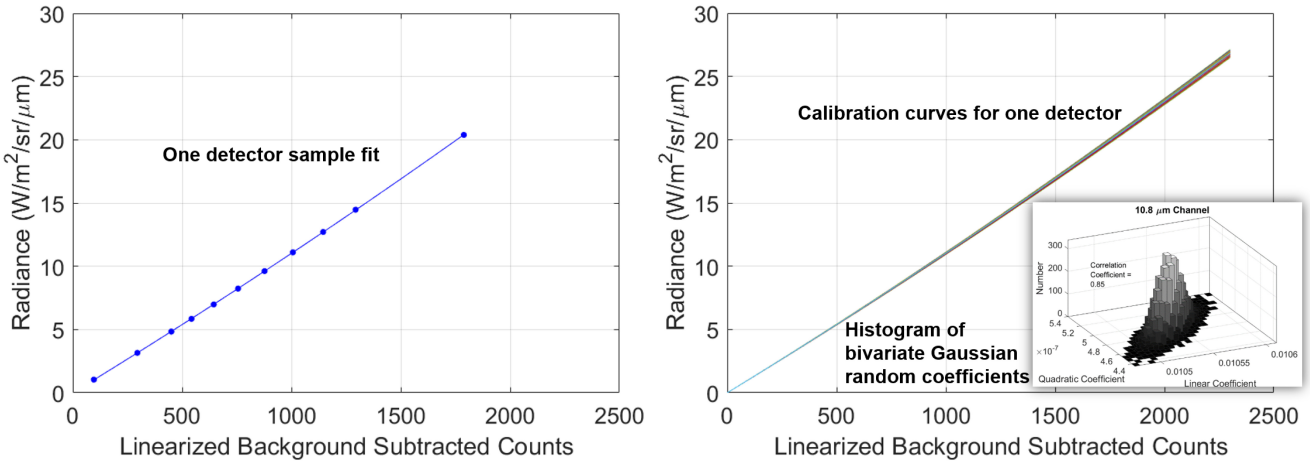

Fig. 5. Illustration of the Monte Carlo process with correlations. (a) Example of a quadratic radiance versus linearized background subtracted counts fit for one detector is shown. (b) Range of fits generated with random values of fitting coefficients with a correlation coefficient of 0.85 and with their $k = 1$ uncertainties. The inset shows the histogram of the coefficients used to illustrate their bivariate Gaussian distribution.

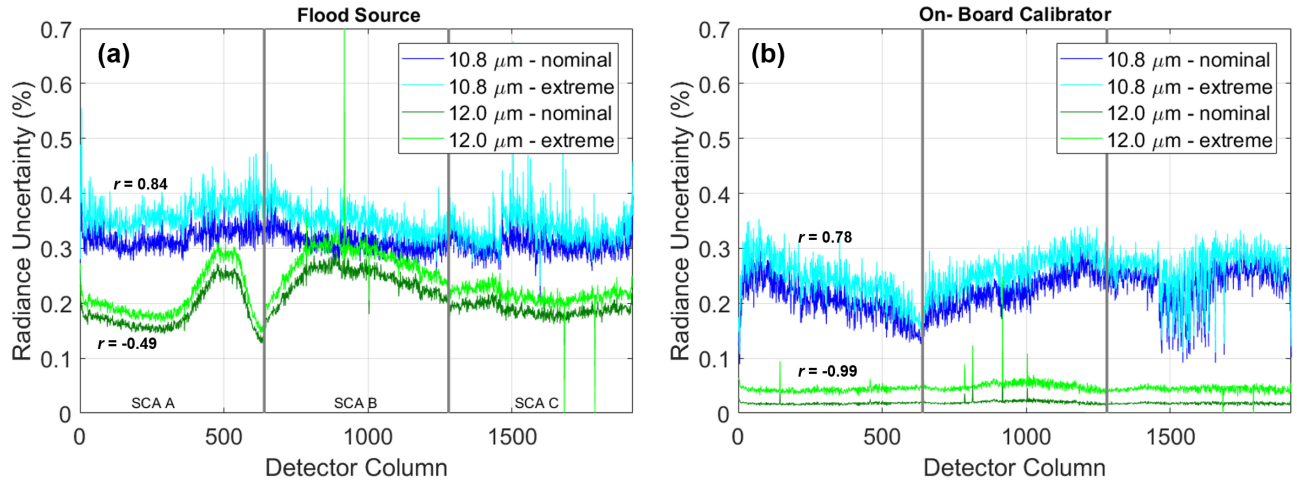

Fig. 6. Results of the Monte Carlo-derived fit uncertainties for (a) flood-source-based calibration and (b) onboard calibration in the nominal and extended brightness-temperature ranges for each channel. The correlation coefficients of the fitting coefficients (r) are responsible for either increasing or reducing the uncertainties. Note that the uncertainty for all SCAs is included (refer to Fig. 1 for the SCA layout).

The calibration reproducibility in the nominal conditions was also characterized through the repeated measurements at the selected flood-source temperatures. The fit to the 11 flood-source temperature points was used to generate the original quadratic fit. This fit was then applied to the signal at the repeated measurements at the temperatures of 260, 270, 290, and 300 K. The radiometric difference between the original and repeated points shows a clear positive mean bias of 0.22% and 0.24% over all detectors and temperatures with an uncertainty of 0.24% and 0.10% for the 10.8- and 12.0-μm bands, respectively, (Fig. 7). The uncertainty of the bias is simply the standard deviation, because we are evaluating each detector individually (the standard deviation of the mean does not tell us how well we know the bias). Note that this term was not evaluated at the extended temperatures, since these points were not repeated for this test.

To review the RSR uncertainty as derived in [25], we observe all the terms in (2a) and (2b), which includes the reference-detector signal uncertainty and TIRS-2 noise. We also included the monochromator wavelength calibration uncertainty, which was determined to be 1 nm by measuring two reference absorption lines of an NIST standard reference material 1921B [41] closest to the TIRS-2 spectral channels, and therefore considered negligible. (Note that a third spectral line at 9.352 μm showed a 15-nm bias, but this was neglected, since its wavelength was far outside the TIRS-2 bands.) Another source of wavelength uncertainty, however, is a consequence of the dispersion across the monochrometer slit. The RSR is calculated using the TIRS-2 pixels near the maximum signal, which does not exactly correspond to the monochromator wavelength setting. Since this setting corresponds to the center of the slit image, a wavelength correction is applied equal to the distance between the location with the maximum signal and the center of the slit in wavelength. The uncertainty of this correction is 1.5 pixel rows or 15 nm in wavelength. We incorporated the uncertainty contributions of

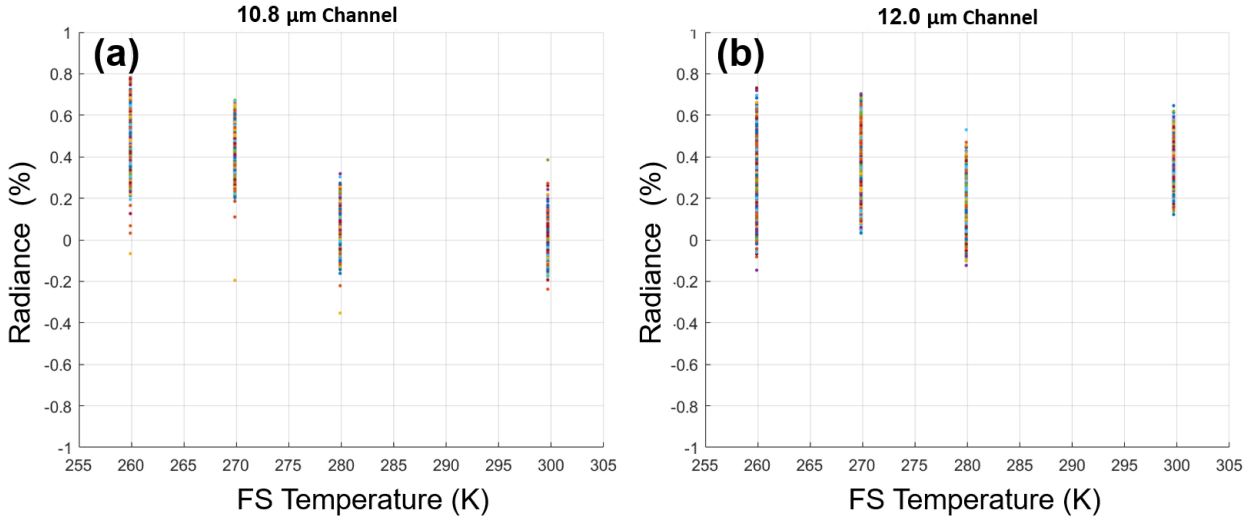

Fig. 7. Reproducibility of the radiometric flood-source-based calibration expressed, as a percent difference is shown for all detector columns in an operational row for (a) 10.8- and (b) 12.0-μm channels.

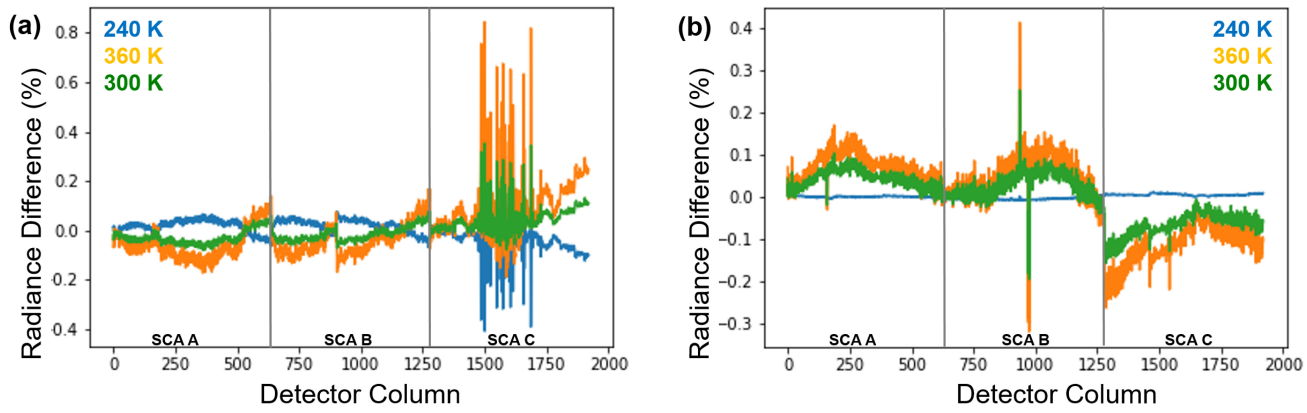

Fig. 8. Spectral uniformity for cold (240 K), nominal (300 K), and high (360 K) brightness-temperature blackbody targets for (a) 10.8- and (b) 12.0-μm channels shown for an operational detector in each column across all SCAs.

the reflectance/transmittance spectra of the optical components or reference-detector response by using 10% of their maximum change within the channels (since these uncertainties were not provided by the vendors). The TIRS-2 noise term is calculated as the standard deviation of the mean for a typical pixel over its samples calculated per wavelength. Incorporating the RSR nonuniformity across all locations gives the uncertainty introduced by using an average RSR per band to represent all detectors as is planned operationally (Fig. 8). This effect and the wavelength uncertainty dominate the spectral uncertainty. The radiometric uncertainties from the combined spectral uncertainty are 0.05% (nominal) and 0.06% (extended) for the 10.8-μm channel and 0.10% (nominal) and 0.15% (extended) for the 12.0-μm channel.

The onboard calibration uncertainties are derived with a similar approach as the flood-source-based calibration uncertainties. The main difference is that we establish the traceability of the OBC calibration by relating the on-orbit OBC-based calibration to the flood-source-based calibration. Using the same calibration equation, we derive the coefficients and their uncertainties independently of the OBC-based calibration. The blackbody operates in a more limited range of temperatures 270–320 K than the flood source. The fitting uncertainties derived through Monte Carlo analysis are 0.27% (nominal) and 0.36% (extended) for the 10.8-μm channel and 0.19% (nominal) and 0.35% (extended) for the 12.0-μm channel. The low uncertainties for the latter channel are due to the strong anticorrelation between the quadratic and linear coefficients (correlation coefficient $= -0.99$) compared with the strong positive correlation in the former channel (correlation coefficient $= 0.78$), as shown in Fig. 6(b).

The flood-source-based and OBC-based calibration curves are compared for all detectors (Fig. 9). By taking the maximum differences in the nominal and extended ranges, we derived the biases of 0.42% and 0.49% in the nominal and extended regions, respectively, for the 10.8-μm channel and 0.32% and 0.40% in the nominal and extended regions, respectively, for the 12.0-μm channel. Note that the biases over the range of blackbody temperature values for the 12.0-μm channel have more variability than that for the 10.8-μm channel.

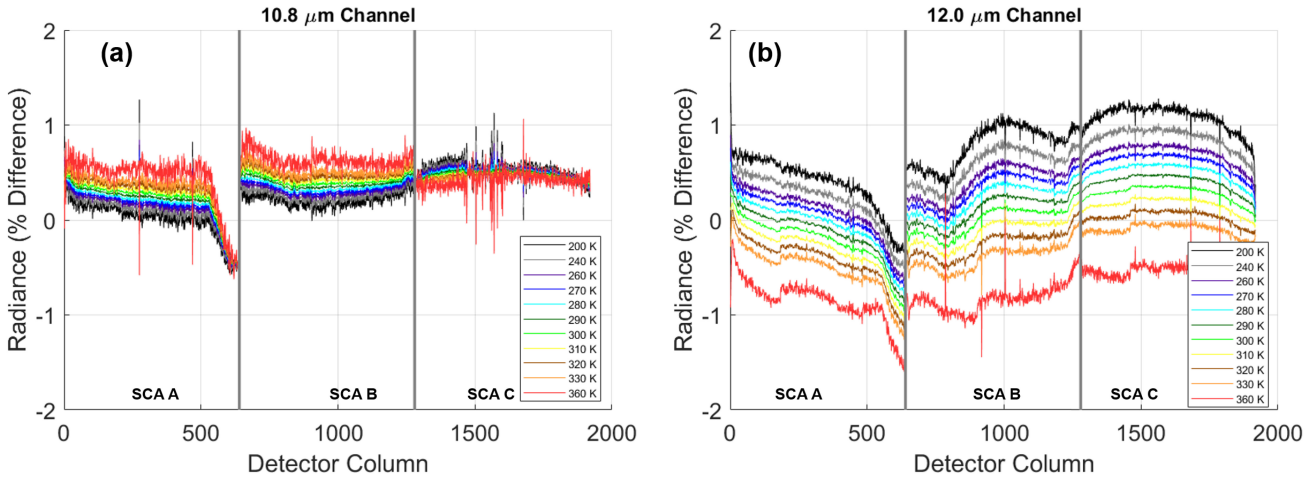

Fig. 9. Radiometric difference between the flood-source- and onboard-based calibrations across all detector columns across all SCAs for an operational row for (a) 10.8-and (b) 12.0-μm channels.

The sharp discontinuities are associated with a change in SCA (Fig. 1), since the detectors on different arrays have larger response differences than the high-frequency differences normally observed between the columns within an SCA. These small response differences generate fits with slightly different uncertainties. The uncertainties of the biases are 0.20% (nominal) and 0.22% (extended) for the 10.8-μm channel and 0.31% (nominal) and 0.32% (extended) for the 12.0-μm channel. Note that during the operations, these biases can potentially be corrected, and we briefly discuss one approach to making this correction, but leave them uncorrected in the uncertainty budget to show a conservative estimate. For instance, consider the background term in (1a) for both the flood-source and OBC views. The radiance difference can be used as a correction term representing the background difference between these two views. This difference varies with the OBC/flood-source temperature and the detector column. Optimally, this background difference would correspond to the same blackbody temperature difference for each channel, but we found that using different background temperature differences for each channel optimized the correction. This could be due to different view factors or emissivity values from the background source in each channel, which can lead to an apparent temperature difference. If we derive these differences for all detectors and channels, the OBC calibration equation can be corrected to obtain the flood-source-based calibration. This correction may be sensitive to the actual on-orbit thermal conditions, so further on-orbit analysis would be recommended before implementing such a correction.

The OBC has four temperature sensors that are averaged to determine its temperature and then converted into effective spectral radiance. The radiometric uncertainty due to the temperature uncertainty is calculated using the same approach as the flood source. The uncertainties are 0.21% (nominal) and 0.36% (extended) for the 10.8-μm channel and 0.19% and 0.35% for the 12.0-μm channel. To characterize any potential impacts to a small change in the OBC view angle, a special test was conducted viewing the OBC at its nominal view angle and through an angle of $\pm 0.5^\circ$ its nominal angle. We found that this effect introduces a negligible uncertainty of 0.02%, indicating a highly Lambertian source in this range of view angles.

Like the flood-source-based calibration reproducibility term, the OBC calibration was characterized through repeated measurements. Since all temperature values were repeated, we compared the calibration curves generated with two independent sets of acquisitions. These fits were then compared through their radiometric differences. The results show a slight positive bias through most of the brightness-temperature range: mean bias of 0.071% and 0.075% over all detectors and temperatures with an uncertainty of 0.34% and 0.54% for the 10.8 and 12.0-μm bands, respectively.

All uncertainty terms without bias are combined according to (3). The bias terms are added separately, and the final $k = 1$ confidence intervals are formed using (4) and (5) and are shown in Table II. For the uncorrected bias terms, there is both a bias listed as well as the bias uncertainty. The biases cause an asymmetric uncertainty interval under the requirements for the nominal and extended regions for both channels. The combined prelaunch uncertainties include terms associated with the flood-source and spectral measurements. The on-orbit calibration includes OBC measurement terms as well as several terms included in the prelaunch uncertainty: linearization, RSR, and TIRS-2 noise. The uncertainty terms contributing to the prelaunch and on-orbit totals are depicted on the figure next to the table. The on-orbit total uncertainty can be considered worst case, since in the operations, there will likely be a method for correcting the bias between the onboard and prelaunch calibrations, which is not included here but will be a subject of future investigation using the on-orbit data. Thus, these combined uncertainties can be thought of as giving the likely range of uncertainties during the operations. For the worst case (on-orbit uncertainty), the largest edge

of the interval is 1.3% (nominal) and 1.7% (extended)—well under the required 2% and 4% values for the on-orbit values. Note that even if we had considered nonuniform scenes in the uncertainty budget, which would include both far-field and near-field stray-light (ghosting) artifacts, these values would increase to 1.9% (nominal) and 2.2% (extended). This includes the contributions from the far-field stray light of 0.57% and 0.83% for the nominal and extended temperature ranges, respectively. This assumes a simple correction using an out-of-field temperature of 293 K. More sophisticated corrections, such as those used for TIRS, could also be employed to reduce these uncertainties further [18]. The uncertainty contributions from ghosting are 0.50% (nominal) and 0.88% (extended). As mentioned, the stray-light artifacts will be discussed in more detail in a separate work.

Although this uncertainty analysis is meant to be comprehensive, it neglects several parameters. For instance, the electronics and detector temperature dependence on the calibration have not been discussed here, although it has been characterized in the case when TIRS-2 is operated in the non-nominal conditions. The onboard calibration methodology may be changed to include corrections to match the flood-source-based calibration more closely. The blackbody degradation over the lifetime of the mission is neglected here, since it cannot be accurately estimated; the TIRS OBC (with the same design as TIRS-2) radiance has experienced an on-orbit degradation of 0.2% and 0.1% per year for the 10.8- and 12.0-μm channels, respectively, but this could be due to the reduction in the detector sensitivities or blackbody degradation [17]. This article also does not consider more complex calibration models in order to simplify the analysis and interpretation of the results.

V. Conclusion

Through extensive prelaunch testing, TIRS-2 has been characterized and calibrated and has demonstrated the performance necessary to meet its radiometric uncertainty requirements. TIRS-2 has established SI traceability through its prelaunch testing and has demonstrated an accurate onboard calibration capability. The prelaunch TIRS-2 radiometric uncertainty is less than 0.80% for the 10.8-μm channels and 0.58% for the 12.0-μm channels over the source temperatures of 260–330 K corresponding to a brightness-temperature uncertainty of about 0.5 and 0.4 K for the two channels. The uncertainty analysis method implemented provides a general framework for addressing the calibration nonlinearity, correlated parameters, and uncorrected biases—commonly encountered in the prelaunch calibration of the remote sensing systems. The expected performance of TIRS-2 is established to give the Landsat data users the confidence to continue using the Landsat thermal imagery for many important environmental applications after its launch and will also serve as a baseline for the future on-orbit validation work. It is expected to meet its users' needs for a variety of environmental applications to continue the Landsat's legacy of providing a high-quality thermal imagery.

Acknowledgment

The authors would like to thank the TIRS-2 Goddard Space Flight Center team for testing support, especially J. Love for software support. They would also like to thank B. Markham and R. Levy of the Landsat Cal/Val team for the helpful discussions and the Space Dynamics Laboratory including Alan Thurgood for blackbody characterization.

References

[1] S. Foga *et al.*, "Cloud detection algorithm comparison and validation for operational landsat data products," *Remote Sens. Environ.*, vol. 194, pp. 379–390, Jun. 2017.

[2] M. J. Wilson and L. Oreopoulos, "Enhancing a simple MODIS cloud mask algorithm for the landsat data continuity mission," *IEEE Trans. Geosci. Remote Sens.*, vol. 51, no. 2, pp. 723–731, Feb. 2013.

[3] M. C. Anderson, R. G. Allen, A. Morse, and W. P. Kustas, "Use of landsat thermal imagery in monitoring evapotranspiration and managing water resources," *Remote Sens. Environ.*, vol. 122, pp. 50–65, Jul. 2012.

[4] R. G. Allen *et al.*, "Automated calibration of the METRIC-Landsat evapotranspiration process," *JAWRA J. Amer. Water Resour. Assoc.*, vol. 49, no. 3, pp. 563–576, May 2013.

[5] C. Santos, I. J. Lorite, R. G. Allen, and M. Tasumi, "Aerodynamic parameterization of the satellite-based energy balance (METRIC) model for ET estimation in rainfed olive orchards of Andalusia, Spain," *Water Resour. Manage.*, vol. 26, no. 11, pp. 3267–3283, Jun. 2012.

[6] X.-L. Chen, H.-M. Zhao, P.-X. Li, and Z.-Y. Yin, "Remote sensing image-based analysis of the relationship between urban heat island and land use/cover changes," *Remote Sens. Environ.*, vol. 104, no. 2, pp. 133–146, Sep. 2006.

[7] M. El-Hattab, A. S. M., and L. G. E., "Monitoring and assessment of urban heat islands over the southern region of Cairo Governorate, Egypt," *Egyptian J. Remote Sens. Space Sci.*, vol. 21, no. 3, pp. 311–323, Dec. 2018.

[8] C. Quintano, A. Fernandez-Manso, and D. A. Roberts, "Burn severity mapping from Landsat MESMA fraction images and land surface temperature," *Remote Sens. Environ.*, vol. 190, pp. 83–95, Mar. 2017.

[9] I. Ogashawara, L. Li, and M. J. Moreno-Madriñán, "Spatial-temporal assessment of environmental factors related to dengue outbreaks in São Paulo, Brazil," *GeoHealth*, vol. 3, no. 8, pp. 202–217, Aug. 2019.

[10] D. P. Roy *et al.*, "Landsat-8: Science and product vision for terrestrial global change research," *Remote Sens. Environ.*, vol. 145, pp. 154–172, Apr. 2014.

[11] D. Reuter *et al.*, "The thermal infrared sensor (TIRS) on Landsat 8: Design overview and pre-launch characterization," *Remote Sens.*, vol. 7, no. 1, pp. 1135–1153, Jan. 2015. [Online]. Available: http://www.mdpi.com/2072-4292/7/1/1135

[12] X. Yu, X. Guo, and Z. Wu, "Land surface temperature retrieval from Landsat 8 TIRS—Comparison between radiative transfer equation-based method, split window algorithm and single channel method," *Remote Sens.*, vol. 6, no. 10, pp. 9829–9852, 2014. [Online]. Available: http://www.mdpi.com/2072-4292/6/10/9829

[13] J. A. Sobrino, F. D. Frate, M. Drusch, J. C. Jimenez-Munoz, P. Manunta, and A. Regan, "Review of thermal infrared applications and requirements for future high-resolution sensors," *IEEE Trans. Geosci. Remote Sens.*, vol. 54, no. 5, pp. 2963–2972, May 2016.

[14] M. Montanaro, A. Gerace, A. Lunsford, and D. Reuter, "Stray light artifacts in imagery from the Landsat 8 thermal infrared sensor," *Remote Sens.*, vol. 6, no. 11, pp. 10435–10456, Oct. 2014. [Online]. Available: http://www.mdpi.com/2072-4292/6/11/10435

[15] M. Jhabvala, D. Reuter, K. Choi, C. Jhabvala, and M. Sundaram, "QWIP-based thermal infrared sensor for the Landsat data continuity mission," *Infr. Phys. Technol.*, vol. 52, no. 6, pp. 424–429, 2009. [Online]. Available: http://www.sciencedirect.com/science/article/pii/S1350449509000619

[16] X. Xiong, B. N. Wenny, A. Wu, and W. L. Barnes, "MODIS onboard blackbody function and performance," *IEEE Trans. Geosci. Remote Sens.*, vol. 47, no. 12, pp. 4210–4222, Dec. 2009.

[17] M. Montanaro, R. Levy, and B. Markham, "On-orbit radiometric performance of the Landsat 8 thermal infrared sensor," *Remote Sens.*, vol. 6, no. 12, pp. 11753–11769, Nov. 2014.

[18] A. Gerace and M. Montanaro, "Derivation and validation of the stray light correction algorithm for the thermal infrared sensor onboard Landsat 8," *Remote Sens. Environ.*, vol. 191, pp. 246–257, Mar. 2017. [Online]. Available: http://www.sciencedirect.com/science/article/pii/S0034425717300421

[19] J. McCorkel *et al.*, "Landsat 9 thermal infrared sensor 2 characterization plan overview," in *Proc. IEEE Int. Geosci. Remote Sens. Symp. IGARSS*, Jul. 2018, pp. 8845–8848.

[20] J. Barsi, J. Schott, S. Hook, N. Raqueno, B. Markham, and R. Radocinski, "Landsat-8 thermal infrared sensor (TIRS) vicarious radiometric calibration," *Remote Sens.*, vol. 6, no. 11, pp. 11607–11626, Nov. 2014.

[21] M. Montanaro, A. Gerace, and S. Rohrbach, "Toward an operational stray light correction for the Landsat 8 thermal infrared sensor," *Appl. Opt.*, vol. 54, no. 13, p. 3963, 2015.

[22] R. U. Datla, J. P. Rice, K. R. Lykke, B. C. Johnson, J. J. Butler, and X. Xiong, "Best practice guidelines for pre-launch characterization and calibration of instruments for passive optical remote sensing," *J. Res. Nat. Inst. Standards Technol.*, vol. 116, no. 2, p. 621, Mar. 2011.

[23] J. H Hair *et al.*, "Landsat 9 thermal infrared sensor 2 architecture and design," in *Proc. IEEE Int. Geosci. Remote Sens. Symp. IGARSS*, Jul. 2018, pp. 8841–8844.

[24] B. Efremova *et al.*, "Landsat 9 thermal infrared sensor 2 subsystem-level spectral test results," in *Proc. IEEE Int. Geosci. Remote Sens. Symp. IGARSS*, Jul. 2018, pp. 8849–8852.

[25] A. J. Pearlman, B. Efremova, A. Lunsford, J. McCorkel, A. Simon, and D. Reuter, "Landsat 9 thermal infrared sensor 2 spectral response test: Updates and perspective," in *Proc. IEEE Int. Geosci. Remote Sens. Symp. IGARSS*, Jul. 2019, pp. 8534–8537.

[26] S. D. Laboratory, "Tirs flood source 2018 calibration report," Space Dyn. Lab., Logan, UT, USA, Tech. Rep. SDL/18-877, May 2018.

[27] H. Latvakoski, M. Watson, and S. Topham, "Testing of highly accurate blackbodies," in *Infrared Remote Sensing and Instrumentation XIX*, M. Strojnik and G. Paez, Eds. Bellingham, WA, USA: SPIE, Sep. 2011.

[28] J. P. Rice and B. C. Johnson, "The NIST EOS thermal-infrared transfer radiometer," *Metrologia*, vol. 35, no. 4, pp. 505–509, Aug. 1998.

[29] M. Montanaro *et al.*, "Landsat 9 thermal infrared sensor 2 preliminary stray light assessment," in *Proc. IEEE Int. Geosci. Remote Sens. Symp. IGARSS*, Jul. 2018, pp. 8853–8856.

[30] M. Montanaro, A. Lunsford, Z. Tesfaye, B. Wenny, and D. Reuter, "Radiometric calibration methodology of the Landsat 8 thermal infrared sensor," *Remote Sens.*, vol. 6, no. 9, pp. 8803–8821, Sep. 2014.

[31] R. Datla, X. Shao, C. Cao, and X. Wu, "Comparison of the calibration algorithms and Si traceability of MODIS, VIIRS, GOES, and GOES-R ABI sensors," *Remote Sens.*, vol. 8, no. 2, p. 126, Feb. 2016.

[32] X. Xiong and W. Barnes, "An overview of MODIS radiometric calibration and characterization," *Adv. Atmos. Sci.*, vol. 23, no. 1, pp. 69–79, Jan. 2006.

[33] J. McIntire, D. Moyer, H. Oudrari, and X. Xiong, "Pre-launch radiometric characterization of JPSS-1 VIIRS thermal emissive bands," *Remote Sens.*, vol. 8, no. 1, p. 47, Jan. 2016.

[34] E. C. Wack, M. P. Weinreb, and J. D. Lawrence, "Prelaunch infrared calibration of the GOES I-M imager and sounder," in *Earth Observing Systems V*, W. L. Barnes, Ed. Bellingham, WA, USA: SPIE, Nov. 2000.

[35] A. J. Pearlman, F. Padula, C. Cao, and X. Wu, "The GOES-r advanced baseline imager: Detector spectral response effects on thermal emissive band calibration," in *Sensors, Systems, and Next-Generation Satellites XIX*, R. Meynart, S. P. Neeck, and H. Shimoda, Eds. Bellingham, WA, USA: SPIE, Oct. 2015.

[36] BIPM. (Sep. 2008). *GUM 1995 With Minor Corrections: Evaluation of Measurement Data—Guide to the Expression of Uncertainty in Measurement*. [Online]. Available: https://www.bipm.org/utils/common/documents/jcgm/JCGM_100_2008_E.pdf

[37] BIPM. (2008). *Evaluation of Measurement Data Supplement 1 to the 'Guide to the Expression of Uncertainty in Measurement' Propagation of Distributions Using a Monte Carlo Method*. [Online]. Available: https://www.bipm.org/utils/common/documents/jcgm/JCGM_101_2008_E.pdf

[38] K.-F. Chiang, X. Xiong, A. Wu, and W. L. Barnes, "MODIS thermal emissive bands calibration uncertainty analysis," in *Earth Observing Systems IX*, W. L. Barnes and J. J. Butler, Eds. Bellingham, WA, USA: SPIE, Oct. 2004.

[39] P. Z. Peebles, *Probability, Random Variables, and Random Signal Principles*, 4th ed., S. W. Director, Ed. New York, NY, USA: McGraw-Hill, 2001.

[40] S. Phillips, K. Eberhardt, and B. Parry, "Guidelines for expressing the uncertainty of measurement results containing uncorrected bias," *J. Res. Nat. Inst. Standards Technol.*, vol. 102, no. 5, p. 577, Sep. 1997.

[41] D. Gupta, L. Wang, L. M. Hanssen, J. J. Hsia, and R. V. Datla, *Standard Reference Materials: Polystyrene Films for Calibrating the Wavelength Scale of Infrared Spectrophotometers SRM 1921*. Washington, DC, USA: NIST, U.S. Government Printing Office, 1995.

Aaron Pearlman (Member, IEEE) received the B.S. degree in electrical engineering from Tufts University, Medford, MA, USA, in 2001, and the M.S. and Ph.D. degrees in electrical engineering from the University of Rochester, Rochester, NY, USA, in 2003 and 2006, respectively.

He became an IC Post-Doctoral Research Fellow with the National Institute of Standards and Technology, Gaithersburg, MD, USA, to conduct research on single photon generating and detecting technologies for quantum information applications. He has provided prelaunch testing support and technical oversight and coordination for a validation field campaign for the National Oceanic and Atmospheric Administration's (NOAA's) new generation of satellite sensors. In 2017, he joined the NASA Goddard Space Flight Center's Calibration Team to support prelaunch testing for the Landsat Program's Thermal Infrared Sensor-2. He is the Chief Scientist of GeoThinkTank LLC, Washington, DC, USA. His work focuses on characterizing remote sensing systems before launch and developing novel methods for validating their postlaunch performance.

Matthew Montanaro received the B.S. degree in physics and the Ph.D. degree in imaging science from the Rochester Institute of Technology (RIT), Rochester, NY, USA, in 2005 and 2009, respectively.

He is a Senior Research Scientist involved in the calibration of the thermal infrared imaging instruments for the NASA Goddard Space Flight Center and the U.S. Geological Survey. He is also specialized in the calibration of the Thermal Infrared Sensor (TIRS) onboard Landsat 8, both preflight and on-orbit. He serves as the Deputy Calibration Lead for the upcoming Landsat 9/TIRS-2 instrument and serves on the Landsat Calibration & Validation team. In addition, he has supported and advised a number of Imaging Science graduate and undergraduate students through RIT.

Boryana Efremova received the Ph.D. degree in astronomy and astrophysics and the M.S. degree in physics from Sofia University, Sofia, Bulgaria, in 2009.

She has been working in the field of remote sensing instrument calibration since 2011, supporting the prelaunch and/or on-orbit calibration, instrument monitoring, and validation of sensors such as Visible Infrared Imaging Radiometer Suite (VIIRS) onboard the Suomi NPP spacecraft, the Advanced Baseline Imager (ABI) onboard the geostationary GOES-16 and GOES-17 satellites, and the prelaunch calibration and testing of the Landsat 9 Thermal Infrared Sensor 2 (TIRS-2).

Joel McCorkel received the B.S. degree in optical engineering and the Ph.D. degree in optical sciences from the University of Arizona, Tucson, AZ, USA, in 2005 and 2009, respectively.

He is a Physical Research Scientist with Biospheric Sciences Laboratory, NASA Goddard Space Flight Center, Greenbelt, MD, USA, where his work involves the development and characterization of the next-generation environmental monitoring and Earth observing sensors. He serves as the GOES-R Flight Project Scientist, the Landsat 9 TIRS-2 Deputy Instrument Scientist leading the prelaunch instrument characterization, and the Principle Investigator of the Goddard Laser for Absolute Measurement of Radiance (GLAMR) calibration facility.

Brian Wenny (Member, IEEE) received the B.S. degree in physics from Ursinus College, Collegeville, PA, USA, in 1991, and the M.S. and Ph.D. degrees in atmospheric science from North Carolina State University, Raleigh, NC, USA, in 1996 and 2000, respectively.

He worked with the Moderate-Resolution Imaging Spectroradiometer Characterization Support Team (MCST), prelaunch calibration for the Landsat 8 Thermal Infrared Sensor (TIRS) and Landsat 9 TIRS-2 instruments, and the Stratospheric Aerosol and Gas Experiment III (SAGE III). He is a Chief Research Scientist with Science Systems and Applications, Inc. (SSAI), Lanham, MD, USA, working primarily on the RadCalNet project.

Allen Lunsford, photograph and biography not available at the time of publication.

Dennis Reuter, photograph and biography not available at the time of publication.